What Is the Best DFT Functional for Vibronic Calculations? A Comparison of the Calculated Vibronic Structure of the S-1-S-0 Transition of Phenylacetylene with Cavity Ringdown Band…

8 AUTHORS, INCLUDING:

Gary V. Lopez
Brown University
24 PUBLICATIONS **107** CITATIONS

SEE PROFILE

Chih-Hsuan Chang
CiS Forschungsinstitut für Mikrosensorik und …
16 PUBLICATIONS **45** CITATIONS

SEE PROFILE

Gregory E Hall
Brookhaven National Laboratory
127 PUBLICATIONS **2,591** CITATIONS

SEE PROFILE

Trevor Sears
Brookhaven National Laboratory
180 PUBLICATIONS **3,538** CITATIONS

SEE PROFILE

What Is the Best DFT Functional for Vibronic Calculations? A Comparison of the Calculated Vibronic Structure of the S_1–S_0 Transition of Phenylacetylene with Cavity Ringdown Band Intensities

Gary V. Lopez,[†] Chih-Hsuan Chang,[‡] Philip M. Johnson,*,[†] Gregory E. Hall,[‡] Trevor J. Sears,[†,‡] Beatrice Markiewicz,[§] Mariana Milan,[§] and Alexey Teslja[§]

[†]Chemistry Department, Stony Brook University, Stony Brook, New York 11794, United States

[‡]Department of Chemistry, Brookhaven National Laboratory, Upton, New York 11973, United States

[§]Department of Chemistry and Pharmaceutical Science, Fairleigh Dickinson University, New Jersey 07940, United States (Faculty and Student Teams Summer Program, 2010, Office of Science, United States Department of Energy)

ABSTRACT: The sensitivity of vibronic calculations to electronic structure methods and basis sets is explored and compared to accurate relative intensities of the vibrational bands of phenylacetylene in the $S_1(A\ ^1B_2) \leftarrow S_0(X\ ^1A_1)$ transition. To provide a better measure of vibrational band intensities, the spectrum was recorded by cavity ringdown absorption spectroscopy up to energies of 2000 cm^{-1} above the band origin in a slit jet sample. The sample rotational temperature was estimated to be about 30 K, but the vibrational temperature was higher, permitting the assignment of many vibrational hot bands. The vibronic structure of the electronic transition was simulated using a combination of time-dependent density functional theory (TD-DFT) electronic structure codes, Franck–Condon integral calculations, and a second-order vibronic model developed previously [Johnson, P. M.; Xu, H. F.; Sears, T. J. *J. Chem. Phys.* **2006**, 125, 164331]. The density

functional theory (DFT) functionals B3LYP, CAM-B3LYP, and LC-BLYP were explored. The long-range-corrected functionals, CAM-B3LYP and LC-BLYP, produced better values for the equilibrium geometry transition moment, but overemphasized the vibronic coupling for some normal modes, while B3LYP provided better-balanced vibronic coupling but a poor equilibrium transition moment. Enlarging the basis set made very little difference. The cavity ringdown measurements show that earlier intensities derived from resonance-enhanced multiphoton ionization (REMPI) spectra have relative intensity errors.
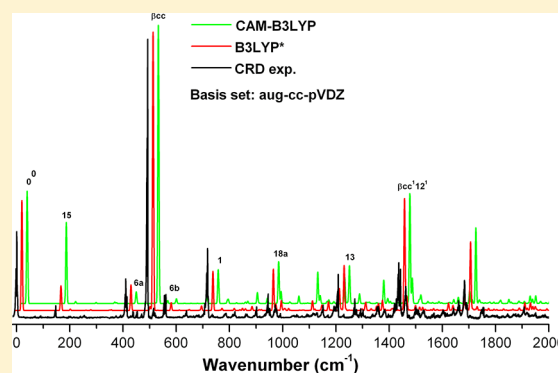
INTRODUCTION

The capability to predict optical spectra has many applications in problems associated with areas such as chemical physics, remote sensing, and astronomy.[1–3] To refine this predictive capacity, one needs to compare methods using the latest theories to accurate experimental data. A key problem in predicting electronic spectra is calculating the interaction of the vibrational and electronic motions. The effects of such vibronic interactions may dominate the observed vibrational patterns of electronic transitions that are optically weak at the equilibrium geometry. In addition to predicting spectra, vibronic calculations can serve as a sensitive test of the quality of the molecular potentials and wave functions produced by electronic structure calculations. Relative vibrational strengths can vary more dramatically with changes in the potential than either electronic or vibrational energies, and can indicate which parts of the potential are in need of improvement.

Calculating the intensities of the vibrational structure in weaker transitions of molecules can be difficult since many different vibrational modes can participate in providing intensity. However, increasing computational power and recent

developments in electronic structure theory and methods now promise the possibility of accurate treatments of medium and large size systems.[4,5] There are choices involved in doing electronic structure calculations, however, and to guide the selection of programs and methods there needs to be a careful comparison of theoretical results with experimental values. Of course, to make a validation worthwhile, the experimental data must be as accurate as possible. Here we test a group of density functional theory (DFT) methods by comparison to the relative vibronic line intensities of a molecule, phenylacetylene (PA), measured with cavity ringdown spectroscopy.

PA is a molecule with an unsaturated group covalently bound to an aromatic benzene ring. It is considered as one of the simplest molecules for modeling the interactions between differently bonded π-electron systems, and its $S_1 \leftarrow S_0$ electronic band system has been the subject of a number of spectroscopic studies.[6–11] It is a C_{2v} symmetry molecule with a

total of 36 nondegenerate normal modes, 13 of which belong to a_1 symmetry, 3 to a_2, 8 to b_1, and 12 to b_2. Three out of the four symmetry types can induce dipole intensity, making its study more challenging. The vibrations below 2000 cm^{-1} are related to different types of CC stretching, CC bending, and ring deformation modes. Although it is formally optically allowed, its first excited state (S_1) derives from the forbidden $^1B_{2u}$ state of benzene, resulting in an intrinsically weak $S_1 \leftarrow S_0$ band system that gains intensity by coupling to nearby strongly allowed A_1 and B_2 states through b_2 and a_1 vibrations.[12] This transition is therefore representative of the interesting and challenging case where the transition is formally allowed, but substantial amounts (sometimes most) of the intensity in the various a_1 vibrations are due to vibronic coupling, and many of the strongest bands are nonsymmetric vibronic inducing modes.

Recent time-delayed ionization studies by Hofstein et al.[13] using a two-color pump−probe photoionization technique revealed unusual photophysics in the S_1 excited state of PA. A species with an unexpectedly long lifetime (>100 μs) was observed under collision-free molecular beam conditions. Rotationally resolved spectroscopic measurements ruled out mechanisms involving molecular clusters whose predissociation could result in the production of long-lived low vibrational levels of the T_1 state on dissociation. The long-lived species is formed directly (at least on a nanosecond time scale) on excitation of the isolated monomer and has a photoelectron spectrum distinct from the short-lived (fluorescent) S_1 state.[13] The accumulated evidence pointed toward formation of a low-energy isomer or some as-yet unknown pathway into the low vibrational levels of T_1.

For PA, accurate published calculations were first reported by Serrano-Andrés et al.[14] and Amatatsu and Hasabe.[15] These were prompted by high-resolution spectroscopic studies from Ribblett et al.[11] that established the symmetry of the S_1 state as $^1B_2$. Previously, Narayanan et al.[10] had erroneously assigned S_1 as $^1A_1$ symmetry based on resonant two-photon ionization (R2PI) spectra and lower level ab initio calculations. Pugliesi et al.[16] used extensive ab initio calculations, together with experimentally determined rotational constants, to investigate the character of the three lowest lying electronic states of the molecule and to model the Franck−Condon (but not the vibronic) activity in the S_1−S_0 spectrum. Their work emphasized the need for accurate treatment of configuration interaction between two nearly degenerate excitations involving the four orbitals around the Fermi level. According to Platt's classification,[17] the minus combination of these configurations results in a spectrally weak lower energy state with ^1L_b character, while the S_2 state, ^1L_a, is predominantly the lowest unoccupied molecular orbital (LUMO) ← highest occupied molecular orbital (HOMO) excitation.

Our group[12,18] has used resonance-enhanced multiphoton ionization (REMPI) spectroscopy with velocity map imaging detection of the photoelectron spectrum of the excited vibronic state to investigate the possibility that specific vibrational motions may promote the production of the long-lived species. The vibronic spectrum was compared to computed spectra based on quantum chemical calculations and the vibronic intensity model of Johnson et al.[18] Vibronic intensity calculations were essential for deciding between alternative possible spectral assignments. However, it was found that in order to match the calculated intensity, contributions from differently polarized transition moments needed to be scaled. It

is possible that partial saturation of the REMPI signals for strong bands, or differences in ionization cross sections for different symmetry modes, might at least partly explain the discrepancy, and the present experimental work was initiated to measure reliable absolute and relative vibronic band absorption intensities to compare to the calculations.

In recent theoretical calculations on other small and medium-sized aromatic molecules,[4] doubts have also been raised about the accuracy of commonly used time-dependent DFT (TD-DFT) methods for the calculation of some excited states.[5,19] The use of common functionals such as B3LYP can lead to serious errors in the energies for some states of ^1L_a symmetry (for example S_2 of PA) due to poor estimates of the long-range parts of the electron density function. It was suggested that long-range-corrected (LRC) functionals would be a better choice for some aromatic excited states.

In our previous work,[12] while energies and vibrational frequencies were calculated using MCSCF methods, TD-DFT was used to compute the excited states at the large number different geometries required for the calculation of the transition moment derivatives needed for the intensity calculations. If the TD-DFT wave function for the S_2 state is not reliable, for example in a way that de-emphasizes its true extent, then vibronic coupling in S_1 could be incorrect since the coupling mixes S_1 and S_2. The present calculations use a single method to compute both vibrational energies and transition moments, and explore the use of LRC DFT functionals.

We also report the measurement of the $S_1 \leftarrow S_0$ transition in PA by cavity ringdown (CRD)[20] laser absorption spectroscopy. Spectra were recorded both at ambient temperatures and, most usefully, in a slit-jet cooled environment. The rotational temperature was obtained from a band contour analysis of the jet-cooled sample. Vibrational cooling was less efficient than rotational cooling in the slit jet and the spectrum therefore includes many resolved vibrational hot-bands leading to new information on the ground state vibrational structure.

■ VIBRONIC INTENSITY CALCULATIONS

The method applied to obtain the vibronic intensities to second-order in the transition moment expansion has been described previously.[18] For many vibrations of PA, it is found that the first- and second-order contributions are similar in magnitude.

To simulate the vibronic spectra of PA, the ground and excited state geometries, vibrational frequencies, and transition moments were all calculated with the same functional and basis set. The ground state was calculated using standard DFT, and the excited states were calculated with TD-DFT using Gaussian 09.[21] Functionals explored were B3LYP, CAM-B3LYP, and LC-BLYP. Basis sets were aug-cc-pVDZ and aug-cc-pVTZ, and all the electronic structure calculations presented here were carried out on Quad-core AMD Opteron Processor 8379 HE 2.4 GHz workstations with 16 processors using the Gaussian 09[21] electronic structure packages. The calculated transition moments were combined with Franck−Condon integrals from MolFC (a program developed and distributed by Borrelli and Poluso[22]) using a vibronic interaction program written in LabVIEW.

Intensities were calculated for every symmetry-viable vibrational level up to about 2000 cm^{-1} (~15 000 states) for the in-plane polarized (a_1 and b_2) and the out-of-plane polarized (a_2) symmetries.

▪ EXPERIMENTAL METHODS

A pulsed Nd:YAG laser (Pro 290, Spectra-Physics) was used to pump an optical parametric oscillator (MOPO-HF, Spectra-Physics). The output of the MOPO laser was doubled in a type I β-barium borate (BBO) crystal and directed into a 92.5 cm long ringdown cavity with two highly reflective (R = 0.998), 267−287 nm spectral range, concave mirrors. A photo-multiplier tube (PMT, Hamamatsu 1P28) was located behind the exit mirror to monitor the light leaking out of the cavity. A wavemeter (Coherent WaveMaster) was used to calibrate the wavelength, and irises were mounted along the beam path for day-to-day alignment, as well as to restrict the cross-sectional area of the beam. A delay generator (Stanford Research Systems DG535) provided a timing sequence for the pulsed valve and laser system, and triggered a 300 MHz the oscilloscope (LeCroy 9310M). PA (98%) purchased from Farchan Division Chemsampco, Inc. was used without further purification and introduced into the central portion of the vacuum chamber using Argon (400 Torr backing pressure) as the carrier gas. For the jet-cooled experiments, a pulsed slit valve (1 cm long, General Valve Corporation, model 99), and two turbomolecular pumps (Edwards) were used to evacuate the chamber to pressures less than 10^{-6} Torr. The slit-jet aperture was held approximately 2 cm from the laser beam axis. Chamber pressure during operation of the nozzle was typically 4×10^{-5} Torr.

▪ RESULTS AND DISCUSSION

Cavity Ringdown. The cavity ringdown experiment was described in a recent publication.[23] Briefly, two different decay
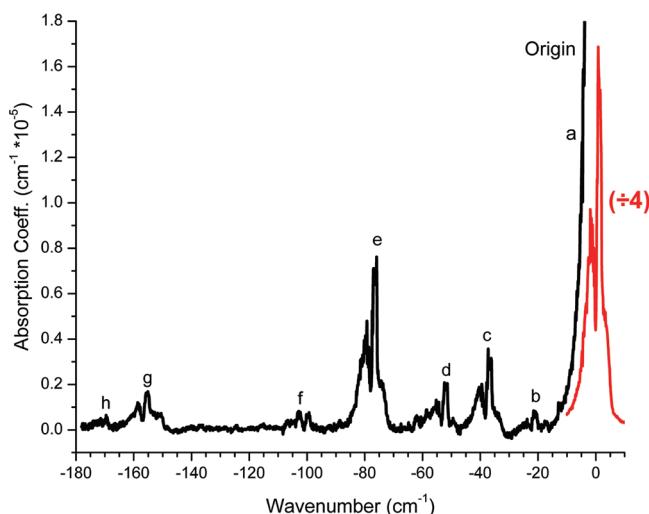

Figure 1. Hot bands on the red side of the band origin in the slit jet CRD spectrum of the $S_1 \leftarrow S_0$ transition of PA (the full origin band has been reduced by a factor of 4). See Table 1 for assignments.

waveforms that correspond to an empty cavity and to PA absorption were obtained at room temperature. The empty cavity decay curve was recorded by averaging 200 waveforms on the oscilloscope, and the PA absorption decays were recorded using a 50 shot average per wavelength step. Neglecting the first few points that typically contained some systematic noise, the signals were fit using a nonlinear least-squares Levenberg−Marquardt fitting algorithm with analytical derivatives to the formula

$$V(t) = V_0 e^{-t/\tau} \tag{1}$$

to extract the ringdown time, τ.

The general equation to convert a measured ringdown decay time (τ) to an absorption coefficient (α) is

$$\alpha = N\sigma = \frac{1}{c}\left(\frac{1}{\tau} - \frac{1}{\tau_0}\right) \tag{2}$$

where c is the speed of light, τ_0 corresponds to the empty cavity decay lifetime, τ corresponds to the ringdown time when an absorbing species is present, σ is the absorption cross-section in cm^2, and N is the number density in molecules cm^{-3}. A major attribute of CRD spectroscopy is that the ringdown time, and thus the absorption coefficient, should be invariant with respect to fluctuation in laser intensity and mode quality. However, tests showed that PMT saturation could lead to apparent systematic changes in measured ringdown times, so care was taken to avoid saturation.

The room temperature spectrum in the region near the band origin can be found in a recent publication.[23]

Jet-Cooled Spectrum. The complete spectrum was recorded from 180 cm^{-1} below the band origin to 2000 cm^{-1} above, i.e., from approximately 35 700 cm^{-1} to 37 900 cm^{-1} using a slit jet-cooled sample. Background subtraction was performed by averaging a waveform at each laser wavelength, at two laser time delays relative to the pulsed valve trigger. The first recorded the signal with gas present, while the second corresponded to the empty chamber at the same laser wavelength position. This method is preferable because any changes in the cavity alignment are accounted for.

To estimate the rotational temperature of the jet-cooled spectrum, the origin band rotational contour was simulated using a LabVIEW-based interface that calls a previously developed asymmetric rotor code.[24] The rotational constants of Ribblett et al.[11] were used in the simulations. The CRD rotational contours of the PA origin band (an a_1 symmetry vibration leading to type-b rotational selection rules) and the strong βCC band at ν_0^0 + 493 cm^{-1} (a b_2 symmetry band leading to type-a rotational selection rules) were compared to simulated band contours at different temperatures. From these results we estimate the rotational temperature of the molecules in the slit jet-cooled beam was around 30 ± 5 K. The appearance of multiple hot-bands to the red side of the band origin observed in Figure 1 shows that the vibrational cooling is much less than rotational cooling.

The rotational contour simulation of the origin leads to an estimate of 35 878.1 cm^{-1} for the electronic band origin. This value is close to the 35 877.18 cm^{-1} measured by Ribblett et al.[11] in the fully rotationally resolved molecular beam spectrum. The modes 15, 6a, βCC, 6b, and 1 appear as the strong bands in the spectrum below 1000 cm^{-1}. The vibrational energies of these modes are 147, 410, 493, 561, and 718 cm^{-1}, respectively. Even though it is a vibronically induced band, βCC (b_2 symmetry) is the strongest band in this spectrum. Fundamental bands or combination bands involving the low frequency modes can be found as the intensity scale is expanded in the spectrum. Most of these features have been assigned and are in good agreement with our previous study using REMPI and theoretical calculations.[12]

For a better understanding of the spectrum of the S_1 state of PA, we have assigned the hot bands observed near the $S_1 \leftarrow S_0$ band origin shown in Figure 1 by comparing the value obtained

Table 1. Assignments of the Hot Bands near the Band Origin of S$_1$ PA^a

		S$_0$			S$_1$				$\Delta\nu(\nu_{S1} - \nu_{S0})$			hot bands	
		calc. freq.				calc. freq.				calc. freq.			
assignment	symm.	ACCD^d	ACCT^d	exp.^{c}	symm.	ACCD	ACCT	exp.^{c}	ACCD	ACCT	exp.^{e}	freq.	peak label^b
10b	b$_1$	136	144	140[9]	b$_1$	98	93	97[12]	−38	−51	−43	−37	c
15	b$_2$	158	162	152[9]	b$_2$	150	154	147^f	−8	−8	−5	~ −5	a
γCC	b$_1$	354	375	349[9]	b$_1$	265	292	273^f	−89	−83	−76	−76	e
16b	b$_1$	555	563	530[6]	b$_1$	378	381	362[6]	−177	−182	−168	−169	h
16a	a$_2$	418	418	417[6]	a$_2$	264	251	262^f	−154	−167	−155	−155	g
6a	a$_1$	473	477	463[9]	a$_1$	408	412	410^f	−65	−65	−53	−52	d
γCH	b$_1$	609	687	613[6]	b$_1$	493	508	514^f	−116	−179	−99	−99	f
βCC	b$_2$	534	547	514[6]	b$_2$	435	448	493^f	−99	−99	−21	−21	b
4	b$_1$	718	722	689[6]	b$_1$	532	618	586[6]	−186	−104	−103		
11	b$_1$	793	797	756[6]	b$_1$	603	622	710[6]	−190	−175	−170		

^{a}Experimental and calculated frequencies are in wavenumbers. Calculated frequencies were obtained with CAM-B3LYP. ^{b}See Figure 1. ^{c}Experimental freq. from CRD,^{e} King and So,[6] Bacon et al.[9] and REMPI.[12] ^{d}ACCD: aug-cc-pVDZ, ACCT: aug-cc-pVTZ. ^{e}[(Exp. Freq.)$_{S1}$ − (Exp. Freq.)$_{S0}$]. $^f\gamma$CC, 16a, and γCH were reassigned using CRD. See Table 3.
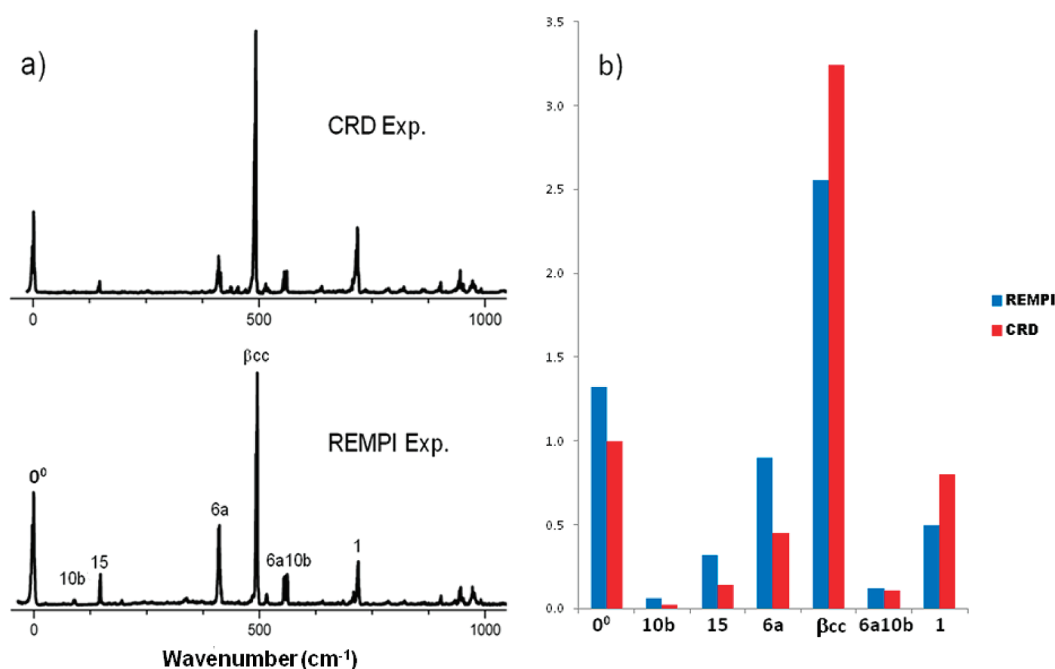

Figure 2. (a) CRD and REMPI assignments of a few strong bands of the S$_1$ PA spectra up to 1000 cm^{-1}. (b) CRD intensities normalized to the origin band and REMPI intensities scaled to make the sum equal to the CRD intensity sum (see Table 2), for the bands labeled in the left-hand panel.

from the difference of the calculated harmonic frequencies of the excited state and the ground state to the frequency offset from the origin of the peak observed in the spectrum. The results presented in Table 1, show that there are difficulties with some previously assigned frequencies. It is likely that the S$_1$ 176, 224, and 470 cm^{-1} peaks assigned by King and So[1] are not γCC, 16a, and γCH.

Using the CRD hot band frequencies, ground state values, and a comparison with the calculated frequencies, new values can be assigned to the γCC, 16a, and γCH modes of S$_1$ as 273, 262, and 514 cm^{-1}, respectively. These modes have little oscillator strength in the cold spectrum and are not readily identifiable there. The 15$^1_1$ transition, labeled "a", is not seen definitively because it is under the origin band, but its position is known accurately from previous work.

From the comparison of a section of the CRD spectrum obtained in this work with our previous REMPI spectrum,[12] it can be seen in Figure 2 that the strongest bands are attenuated in the REMPI spectrum, while weaker bands (including most a$_1$ modes) vary somewhat randomly between techniques. The attenuation of the stronger peaks is related to the fact that they can be affected more by saturation in the nonlinear REMPI process. Also the relative intensities obtained from the REMPI experiment are affected by the laser intensity and various nonlinear and saturation effects as the laser is scanned across a dye region, while in the case of CRD, laser intensity and mode structure do not influence relative absorption strengths. Table 2 compares the relative band intensities from the REMPI and CRD experiments, independently normalized to their origin band intensities. The last column in this table gives a different normalization of the REMPI intensities, scaled instead to match the total intensity of the CRD set. This is illustrated in Figure 2b.

Table 2. Relative Intensities from the REMPI and CRD Experiments, Normalized to the Origin Band Intensities[a]

band	CRD intensity[b]	REMPI intensity[b]	REMPI scaled intensity[c]
0	1.00	1.00	1.32
10b	0.02	0.04	0.06
15	0.14	0.24	0.32
6a	0.45	0.68	0.90
βCC	3.24	1.94	2.56
6a10b	0.11	0.09	0.12
1	0.80	0.37	0.39
Sum	5.76	4.37	

[a]REMPI intensities are also scaled to the same sum as the CRD set and have been plotted in Figure 2b. [b]Normalized to the band origin. [c]Scaled Intensity = REMPI Intensity ($\sum$ CRD Intensity/$\sum$ REMPI Intensity).

Simulated Vibronic Spectra. Theoretical and experimental harmonic fundamental frequencies for the lowest excited singlet state (S_1) of PA are given in Table 3. King and So's[6] numbering system for PA (derived from Wilson's notation[25]) is used for this discussion, while Mulliken's[12] notation is also included for comparison with other work.

The frequencies obtained with all functionals of TD-DFT for the S_1 state of PA are close to the experimental ones, especially in the lower energy part of the spectrum, and no vibrational frequency scaling factor was needed. In previous work at the CASSCF (8,8) level of theory used by Serrano-Andres et al.[14] and Chang et al.,[12] a scaling factor of 0.92 was used. The absence of imaginary frequencies in both S_0 and S_1 states indicates that the C_{2v} planar symmetry is maintained. The ground state of PA has A_1 symmetry, while the first excited state is B_2. A test of basis set sensitivity was done with the B3LYP and CAM-B3LYP functionals using the different sets aug-cc-pVDZ and aug-cc-pVTZ. Table 3 shows that, for most part, there is very little difference in energies between the two basis sets, and the considerable additional expense of the larger set cannot be justified.

A visual comparison of experiment versus calculation depends entirely on peak heights, but the calculated vibronic intensities represent the peak area. To properly compensate for the incomplete rotational resolution of the experimental spectra, the calculated peaks must be adjusted for the peak-to-area ratio of the rotational contours. From 30 K rotational simulations, it is found that the peak-to-area ratio of the b_2 bands is 1.47 times that of the a_1 bands, so the simulated stick spectra were corrected by multiplying the a_1 y-polarized modes by the area correction factor of 1.47. This substantially improves the visual agreement between the experimental and simulated spectra and is included in the simulated spectra shown in Figures 3 and 4.

Table 4 shows the equilibrium transition moments for the S_1–S_0 transition of PA for the different functionals used in this work. The key point is that the LRC functional CAM-B3LYP finds an equilibrium transition moment that is almost 5 times bigger than B3LYP while the LC-BLYP result is yet 36% higher than CAM-B3LYP. This result has a big influence in the calculated intensity of the a_1 vibrations, including the band origin, since the Franck–Condon factors partition this value into the strength of all of them. In terms of the quality of the spectral simulation, this is the crucial difference between using the B3LYP and the LRC functionals, although it has nothing to do with vibronic coupling.

It is desirable to have a more quantitative sense of the quality of the simulated spectra using various functionals. This could be obtained by examining the differences between the calculated intensities of a selected set of the more intense vibrational peaks and their respective CRD intensities, but a direct comparison is not possible because of the lack of absolute CRD absorbances. Also, because of effects such as anharmonic resonances and Coriolis coupling, one should not expect exact agreement between experimental and calculated vibronic intensities, particularly at energies more than 1000 cm^{-1} above the band origin. These perturbations affect the lower intensity peaks more than the larger ones, so it is convenient to weight the percent errors of the bands by the fractional intensity of the transition with respect to the summed intensities of the set. To establish a value representing the quality of the calculations, we proceeded as follows:

1 The sums of the calculated line intensities {CI_i} and the CRD peak values {EX_i} are set equal:

$$\sum_i CI_i = \sum_i EX_i \qquad (3)$$

2 The % errors are taken for each line:

$$Err_i = 100\left(\frac{CI_i - EX_i}{EX_i}\right) \qquad (4)$$

3 The errors are weighted by the fractional experimental line intensities:

$$W_i = \left(\frac{EX_i}{\sum_i EX_i}\right) \qquad (5)$$

4 The weighted mean of the percent error set is

$$\overline{Err_w} = \sum_i W_i|Err_i| \qquad (6)$$

where summations are over the total number of vibronic bands reported in Table 4.

The weighted mean of the percent errors is a useful measure of the quality of the fit.

It is clear from Table 4 that none of the simulations using the various functionals provide a high quality match throughout. The major reasons for the discrepancies vary between functionals, however. For B3LYP calculations, the primary fault lies in the value of equilibrium geometry transition moment (0.014 ea$_0$), with the low value producing a lack of intensity in the a_1 modes, as seen previously.[12]

Examination of the calculated relative vibronic intensities compared to the experiment can indicate potential problem areas in the molecular potential energy surface. For the CAM-B3LYP and LC-BLYP results, the most obvious source of error obtained in both cases is the low energy mode 15. This is the in-plane trans-bending motion of the acetylene group where the terminal carbon has the greatest excursion and the ring undergoes a rotation. The intensity of this mode appears about 6 times as large as it should in the LRC simulations, while it is only twice as big in the B3LYP simulations. This happens because the first-order derivatives for mode 15 (Table 5) have increased in the LRC calculations (while the βCC moment derivatives and the vibrational vectors are about the same). In

Table 3. Theoretical and Experimental Harmonic Fundamental Frequencies (cm^{-1}) for the Lowest Singlet Excited State (S$_1$) of PA

			Theory								experiment			
					TD-DFT									
			Serrano-Andres[b] CASSCF (8,8)	CASSCF (8,8)[d]	B3LYP	LC BLYP	CAM-B3LYP	B3LYP	LC BLYP	CAM-B3LYP			King and So[c]	
notation	Notation		A.N.O.		aug-cc-pVDZ			aug-cc-pVTZ			REMPI	CRD		
symm	Mulliken	King and So[a,c]	scaled freq.*	scaled freq.*	freq.	freq.	freq.	freq.	freq.	freq.	freq.	freq.	freq.	mode description[b]
a$_1$	ν_1	νCH	3334	3325	3475	3510	3490	3461	3488	3474				C$_8$H$_8$ stretch
	ν_2	2	3106	3109	3226	3283	3250	3219	3270	3241				CH stretch
	ν_3	20a	3094	3095	3211	3270	3237	3204	3258	3229				CH stretch
	ν_4	7a	3075	3078	3190	3255	3220	3183	3242	3211				CH stretch
	ν_5	νCC	2036	2032	2115	2270	2187	2111	2267	2184			2061	C$_7$≡C$_8$ stretch
	ν_6	8a	1533	1539	1543	1672	1609	1543	1668	1607				CCH bend
	ν_7	19a	1412	1408	1453	1502	1473	1471	1517	1490	1419			CCH bend
	ν_8	13	1153	1151	1223	1255	1237	1228	1260	1242	1191	1193	1191	C$_1$C$_7$ stretch, CCH bend
	ν_9	9a	1132	1128	1163	1188	1177	1172	1201	1188	1126	1127	1057	CCH bend
	ν_{10}	18a	937	940	996	1031	1008	1001	1035	1014	954	954	951	Ring deformation
	ν_{11}	12	894	898	973	1005	988	982	1020	998	945	945	944	Ring deformation
	ν_{12}	1	690	692	740	754	745	744	759	748	719	718	717	Ring breath
	ν_{13}	6a	413	413	399	417	408	403	421	412	409	410	409	C$_7$C$_8$H$_8$-ring breath
a$_2$	ν_{14}	17a	641	624	747	842	794	752	842	806			728	OP CCH-ring breath
	ν_{15}	10a	566	554	609	672	643	635	688	654			656	OP CCH bend
	ν_{16}	16a	272	265	240	267	264	240	271	251		262	220	OP CCH bend
b$_1$	ν_{17}	5	680	666	852	893	856	860	895	856				OP CCH bend
	ν_{18}	17b	604	588	740	797	762	749	806	773			731	OP CCH bend
	ν_{19}	11	539	527	586	625	603	604	702	622			710	OP CCH bend
	ν_{20}	4	480	464	501	616	532	531	630	618			586	OP CCH bend
	ν_{21}	γCH	400	388	420	521	493	505	524	508		514	470	OP ring deformation
	ν_{22}	16b	295	277	399	368	378	405	373	381			362	OP ring def, C$_7$C$_8$H$_8$ bend
	ν_{23}	γCC	263	160	263	273	265	302	296	292		273	176	OP ring def, C$_7$C$_8$H$_8$ bend
	ν_{24}	10b	109	92	96	102	98	99	109	93	97	91	163	OP ring def, C$_7$C$_8$H$_8$ bend
b$_2$	ν_{25}	7b	3102	3103	3221	3277	3244	3214	3264	3236				CH stretch
	ν_{26}	20b	3084	3085	3199	3257	3224	3193	3245	3215			3079	CH stretch
	ν_{27}	8b	1678	1684	1508	1759	1589	1504	1743	1580	1642	1643		Ring deformation
	ν_{28}	19b	1483	1490	1432	1631	1543	1430	1630	1536	1442	1443		Ring deformation
	ν_{29}	14	1371	1366	1389	1436	1411	1409	1457	1434				CCH bend
	ν_{30}	3	1280	1275	1292	1327	1312	1308	1349	1331	1296	1293		CCH bend
	ν_{31}	9b	1143	1134	1159	1181	1171	1171	1196	1185	1152	1152	1075	CCH bend
	ν_{32}	18b	926	931	1006	1067	1037	1008	1072	1041	990	990	972	CCH bend
	ν_{33}	βCH	719	708	622	730	670	661	764	708				C$_7$C$_8$H$_8$ bend
	ν_{34}	6b	558	559	569	583	574	578	593	583	561	561	560	Ring deformation
	ν_{35}	βCC	513	511	453	456	435	464	470	448	493	493	492	C$_1$C$_7$C$_8$ bend
	ν_{36}	15	144	160	150	153	150	155	157	154	146	147	322	CCH, C$_7$C$_8$H$_8$ bend

Table 3. continued

[a]The symbol ν indicates a stretch, β means an in-plane bend, and γ means an out-of-plane bend. [b]Serrano-Andres et.al.[14] The descriptions are the main contributions to the normal modes. The acetylene carbons are 7 and 8, C_7 is attached to the ring at C_1, while a lack of atom numbering indicates the H or C belongs to the phenyl ring. [c]G. King and S. So.[6] [d]Chang et al.[12] *Scaling factor: 0.92.
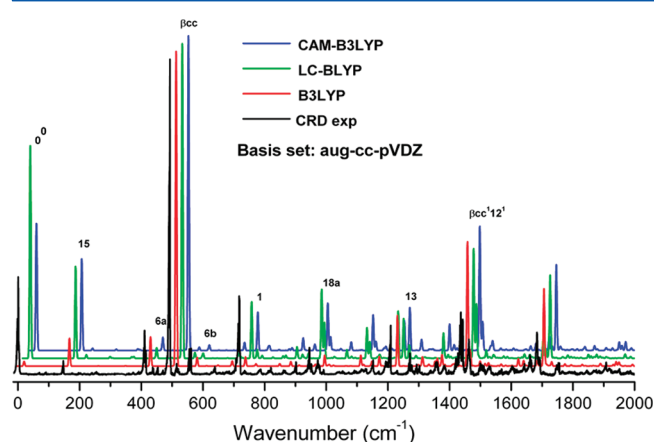

Figure 3. Simulations of the S_1 spectrum of PA up to the second order in vibronic effects, including the area correction factor to the a_1 y-polarized modes. For comparison purposes, spectra are scaled to make the βCC bands equal in height.
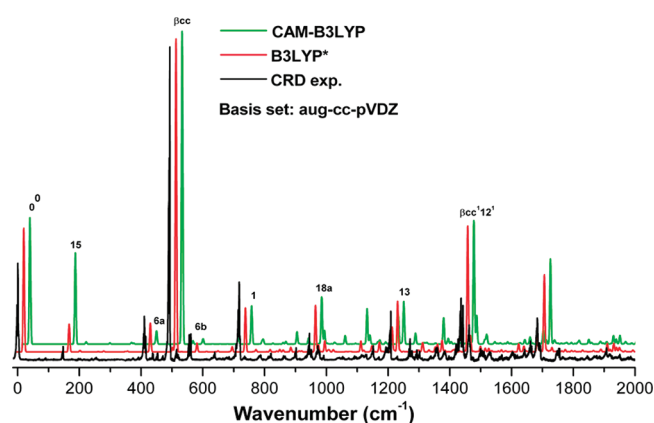

Figure 4. Comparison between the CRD spectrum and the simulated S_1-S_0 absorption spectra of PA with CAM-B3LYP and B3LYP* (where the intensities were calculated using B3LYP transition moment derivatives and the CAM-B3LYP equilibrium transition moment).

the perturbation theory picture of vibronic coupling, this b_2 vibration is mixing in a nearby A_1 electronic state, and is apparently too successful in that effort with the LRC functionals. If mode 15 is removed from the analysis, all the functionals have approximately the same mean error, with CAM-B3LYP being the lowest by a small amount. At higher vibrational energy, mode 13 in the LRC calculations and the combination band $\beta CC^1 12^1$ in all the methods are also anomalously strong.

From the above considerations, it appears that B3LYP generates a poor equilibrium moment but better moment derivatives, while the LRC functionals are just the opposite. Since the equilibrium transition moment enters the vibronic calculations in a simple enough way, it is possible to use the equilibrium moment from one calculation along with the moment derivatives from another to produce a hybrid spectrum. Table 4 therefore contains a column that contains the results of a calculation using the moment derivatives from

B3LYP and the equilibrium moment from CAM-B3LYP (referred to as B3LYP* in Table 4 and Figure 4). This results in a considerably improved mean percent error. The B3LYP* vibronic simulation is compared to the CRD and CAM-B3LYP spectra in Figure 4.

■ SUMMARY AND CONCLUSION

Using any of the functionals, the vibrational structure in the electronic spectra could be fairly accurately simulated for PA, a medium-sized aromatic molecule. The long-range corrected functional CAM-B3LYP provides a 5 times bigger equilibrium transition moment than B3LYP, while the equilibrium transition moment calculated with LC-BLYP higher yet by 36%, increasing the intensities of the a_1 modes in both cases. The increased a_1 intensities are a distinct improvement over our previous calculation[12] using B3LYP moments and MCSCF vibrations, but the relative intensities of certain b_2 vibrations using LRC functionals are less favorable. This may indicate that the LRC functionals do not get the state coupling quite right, or that the vibrational vectors are less than optimal. None of the functionals were without faults. For vibronic calculations on transitions completely forbidden by symmetry, and thus where the equilibrium moment is not an issue, it would appear that B3LYP would be the best choice. For weak allowed transitions, either B3LYP with a CAM-B3LYP equilibrium moment or CAM-B3LYP alone could be used. It should be emphasized, however, that these conclusions are based upon our experience with only PA, and further work on different systems will be necessary to see whether the effects seen in PA are general to a larger class of molecules.

CRD measures the rate of decay of light intensity in a stable optical cavity, and the intensity is related to the direct absorption of the species, which is not affected by the laser intensity. By comparison, REMPI tends to attenuate the intensity of the strong bands because of nonlinear and saturation effects. Since CRD provides a direct absorption spectrum, free of laser intensity effects, results from this technique are very useful for comparison to simulated spectra. The temperature in the argon slit-jet was found to be in the range of 30 ± 5 K, and the appearance of multiple hot-bands to the red of the band origin showed that the vibrational cooling is much less than the rotational cooling. Many of the hot bands observed near the band origin of this transition were assigned.

■ AUTHOR INFORMATION

Notes
The authors declare no competing financial interest.

■ ACKNOWLEDGMENTS

Table 4. Percent Errors of the Calculated Intensities for a Selected Set of the Stronger Vibrational Peaks, with Respect to the CRD Intensities, for the Different DFT Functionals[a]

vibronic band	symm	freq	W_i[b]	B3LYP int.	B3LYP % error[b]	B3LYP*[b] int.	B3LYP* % error[b]	CAM-B3LYP int.	CAM-B3LYP % error[b]	LC-BLYP int.	LC-BLYP % error[b]
$0-0$	a_1	0	0.099	0.007	−93	0.137	39	0.137	39	0.195	98
15^1	b_2	146	0.013	0.039	188	0.031	127	0.099	636	0.084	525
$6a^1$	a_1	409	0.044	0.041	−8	0.032	−28	0.014	−68	0.010	−78
βCC^1	b_2	493	0.318	0.440	38	0.346	9	0.340	7	0.289	−9
βCH^1	b_2	561	0.026	0.012	−53	0.010	−63	0.006	−78	0.005	−82
1^1	a_1	719	0.079	0.001	−98	0.048	−39	0.041	−47	0.052	−34
$6a^2$	a_1	821	0.007	0.013	95	0.001	−92	0.002	−76	0.002	−68
$\beta CC^1 6a^1$	b_2	902	0.012	0.003	−73	0.000	−100	0.007	−46	0.005	−61
12^1	a_1	945	0.027	0.001	−95	0.051	89	0.051	90	0.063	135
$18a^1$	a_1	954	0.010	0.003	−74	0.008	−25	0.015	42	0.033	216
βCC^2	a_1	971	0.014	0.015	8	0.001	−90	0.002	−87	0.001	−89
$9a^1$	a_1	1152	0.014	0.014	−2	0.003	−81	0.004	−68	0.004	−75
13^1	a_1	1191	0.012	0.007	−41	0.027	132	0.032	174	0.043	267
$\beta CC^1 1^1$	b_2	1208	0.049	0.071	44	0.056	13	0.046	−6	0.036	−26
$6b^1 1^1$	b_2	1271	0.021	0.002	−90	0.002	−93	0.001	−93	0.001	−95
$\beta CC^1 12^1$	b_2	1436	0.063	0.174	177	0.134	115	0.134	114	0.100	60
1^2	a_1	1442	0.055	0.023	−58	0.006	−89	0.031	−43	0.050	−8
$\beta CC^1 18b^1$	a_1	1463	0.035	0.007	−80	0.000	−100	0.011	−70	0.001	−98
$18a^1 6b^1$	b_2	1529	0.007	0.005	−34	0.000	−94	0.002	−68	0.002	−74
$\beta CC^1 9a^1$	b_2	1641	0.010	0.001	−88	0.004	−65	0.001	−91	0.001	−93
$1^1 12^1$	a_1	1660	0.018	0.007	−59	0.018	−2	0.015	−14	0.016	−9
$\beta CC^1 13^1$	b_2	1682	0.042	0.108	156	0.085	101	0.003	−94	0.001	−97
$13^1 6b^1$	b_2	1754	0.011	0.003	−73	0.002	−79	0.002	−86	0.002	−86
$18a^2$	a_1	1908	0.012	0.002	−81	0.000	−100	0.003	−78	0.004	−69
equil. trans. mom.				0.0140		0.0669		0.0669		0.0907	
weighted mean % error[b]				71		49		53		59	

[a]Also given are fractional experimental (W_i) and calculated line intensities (int.), weighted mean of the absolute percent errors, and equilibrium transition moments. [b]See text for details.

Table 5. First derivatives of the transition moments for a_1 (y-polarized) and b_2 (z-polarized) vibrational modes

symm.	band	CASSCF-TDDFT[12]	TD-DFT B3LYP (aug-cc-pVDZ)	TD-DFT LC-BLYP (aug-cc-pVDZ)	TD-DFT CAM-B3LYP (aug-cc-pVDZ)	TD-DFT B3LYP (aug-cc-pVTZ)	TD-DFT CAM-B3LYP (aug-cc-pVTZ)
				y-polarized transition moment derivatives			
a_1	6a	0.0880	0.1721	0.1591	0.1668	0.1693	0.1656
	1	0.0560	−0.0926	−0.1001	−0.0985	−0.0934	−0.0999
	12	0.0056	−0.0067	−0.0052	−0.0064	−0.0054	−0.0053
	18a	−0.0115	−0.0101	−0.0061	−0.0080	−0.0136	−0.0113
	9a	0.0044	0.0221	0.0139	0.0159	0.0240	0.0152
	13	0.0226	0.0318	0.0283	0.0279	0.0318	0.0274
	19a	0.0050	−0.0117	−0.0140	−0.0106	−0.0107	−0.0094
	8a	−0.0262	0.0458	0.0049	0.0217	0.0454	0.0228
				z-polarized transition moment derivatives			
b_2	15	0.0623	0.1135	0.2502	0.2399	0.1340	0.2288
	βCC	0.3452	0.7463	0.7519	0.8598	0.6637	0.8376
	6b	−0.1520	−0.1630	−0.1281	−0.1530	−0.1318	−0.1296
	βCH	0.0111	0.0195	0.0334	−0.0091	0.0389	0.0236
	18b	−0.0477	−0.0682	−0.0396	−0.0466	−0.0751	−0.0480
	9b	0.1180	−0.2018	−0.0380	−0.0986	−0.2148	−−0.1033
	3	0.0823	0.1513	−0.0170	0.0243	0.1730	0.0265
	14	−0.0116	−0.0836	0.1087	0.0713	−0.1320	0.0600
	19b	0.2680	0.2233	0.0190	0.1165	0.1161	0.0794
	8b	−0.0445	−0.4014	−0.1027	−0.2504	−0.4012	−0.2675

■ REFERENCES

(1) Reddy, V. S.; Ghanta, S.; Mahapatra, S. *Phys. Rev. Lett.* **2010**, *104*, 111102.

(2) Ghanta, S.; Reddy, V. S.; Mahapatra, S. *Phys. Chem. Chem. Phys.* **2011**, *13*, 14523.

(3) Ghanta, S.; Reddy, V. S.; Mahapatra, S. *Phys. Chem. Chem. Phys.* **2011**, *13*, 14531.

(4) Richard, R. M.; Herbert, J. M. *J. Chem. Theor. Comp.* **2010**, *7*, 1296.

(5) Richard, R. M.; Herbert, J. M. *J. Chem. Theory Comput.* **2011**, *7*, 1296.

(6) King, G. W.; So, S. P. *J. Mol. Spectrosc.* **1971**, *37*, 543.

(7) Powers, D. E.; Hopkins, J. B.; Smalley, R. E. *J. Chem. Phys.* **1981**, *74*, 5971.

(8) Chia, L.; Goodman, L. *J. Chem. Phys.* **1982**, *76*, 4745.

(9) Bacon, A. R.; Hollas, J. M.; Ridley, T. *Can. J. Phys.* **1984**, *62*, 1254.

(10) Narayanan, K.; Chang, G. C.; Shieh, K. C.; Tung, C. C. *Spectrochim. Acta, Part A: Mol. Biomol. Spectrosc.* **1996**, *52*, 1703.

(11) Ribblett, J. W.; Borst, D. R.; Pratt, D. W. *J. Chem. Phys.* **1999**, *111*, 8454.

(12) Chang, C. H.; Lopez, G.; Sears, T. J.; Johnson, P. M. *J. Phys. Chem. A* **2010**, *114*, 8262.

(13) Hofstein, J.; Xu, H. F.; Sears, T.; Johnson, P. M. *J. Phys. Chem. A* **2008**, *112*, 1195.

(14) Serrano-Andres, L.; Merchan, M.; Jablonski, M. *J. Chem. Phys.* **2003**, *119*, 4294.

(15) Amatatsu, Y.; Hasebe, Y. *J. Phys. Chem. A* **2003**, *107*, 11169.

(16) Pugliesi, I.; Watkins, M. J.; Tonge, N. M.; Hornsby, K. E.; Cockett, M. C. R. *Phys. Chem. Chem. Phys.* **2007**, *9*, 5436.

(17) Platt, J. R. *J. Chem. Phys.* **1949**, *17*, 484.

(18) Johnson, P. M.; Xu, H. F.; Sears, T. J. *J. Chem. Phys.* **2006**, *125*, 164331.

(19) Holland, D. M. P.; Shaw, D. A.; Stener, M.; Decleva, P. *J. Phys. B: At., Mol. Opt. Phys.* **2009**, *42*.

(20) O'Keefe, A.; Deacon, D. A. G. *Rev. Sci. Instrum.* **1988**, *59*.

(21) Frisch, M. J., Trucks, G. W., Schlegel, H. B., Scuseria, G. E., Robb, M. A., Cheeseman, J. R., Scalmani, G., Barone, V., Mennucci, B., Petersson, G. A. et al. *Gaussian 09*, revision B.01; Gaussian, Inc.: Wallingford, CT, 2010.

(22) Borrelli, R.; Peluso, A. *J. Chem. Phys.* **2003**, *119*, 8437.

(23) Markiewicz, B.; Milan, M.; Chang, C.; Hall, G.; Teslja, A. To be submitted for publication.

(24) Sears, T. J. *Comput. Phys. Commun.* **1984**, *34*.

(25) Wilson, E. B. *Phys. Rev.* **1934**, *45*.